Electronic Supplementary Material (ESI) for Journal of Materials Chemistry A.

SUPPLEMENTARY INFORMATION

Structure, Defects, and Electrochemistry of Hydrothermally-synthesized Nb-substituted β'-$LiVOPO_4$

Krystal Lee[a,b], Hui Zhou[a], Mateusz Zuba[c], Carol Kaplan[a], Yanxu Zong[c], Linna Qiao[c], Guangwen Zhou[c], Natasha A. Chernova[a], Hao Liu[b,c], M. Stanley Whittingham[a]

[a] NorthEast Center for Chemical Energy Storage (NECCES), Binghamton University, Binghamton, NY 13902-6000, USA

[b] Chemistry Department, Binghamton University, Binghamton, NY 13902-6000, USA

[c] Materials Science and Engineering, Binghamton University, Binghamton, NY 13902-6000, USA

*Email: liuh@binghamton.edu, stanwhit@gmail.com

SEM, ICP-OES, CHNS, TG-MS, FT-IR, XRD of as-synthesized material

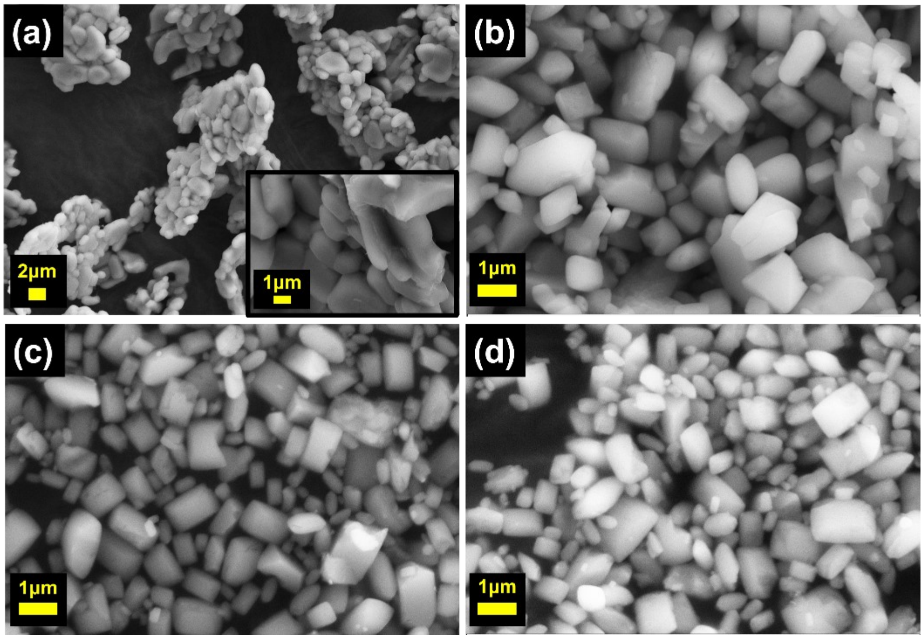

Figure S1. SEM images of (a) pristine HyTA and (b-d) Nb-substituted HyT $LiVOPO_4$ particles.

Table S1. Summary of the elemental composition of Nb-substituted HyT $LiVOPO_4$ determined by ICP-OES, CHNS, and TG-MS measurements.

Sample	Li/P_{ICP}	V/P_{ICP}	Nb/P_{ICP}	P_{ICP}	C/P_{CHNS}	H/P_{CHNS}	H/P_{TG-MS}
3% Nb	0.832(2)	0.968(4)	0.0248(2)	1	0.018(2)	0.777(3)	0.76
5% Nb	0.786(2)	0.933(2)	0.0468(9)	1	0.026(2)	0.827(3)	0.80
7% Nb	0.753(3)	0.919(3)	0.0672(1)	1	0.020(2)	0.794(3)	0.78

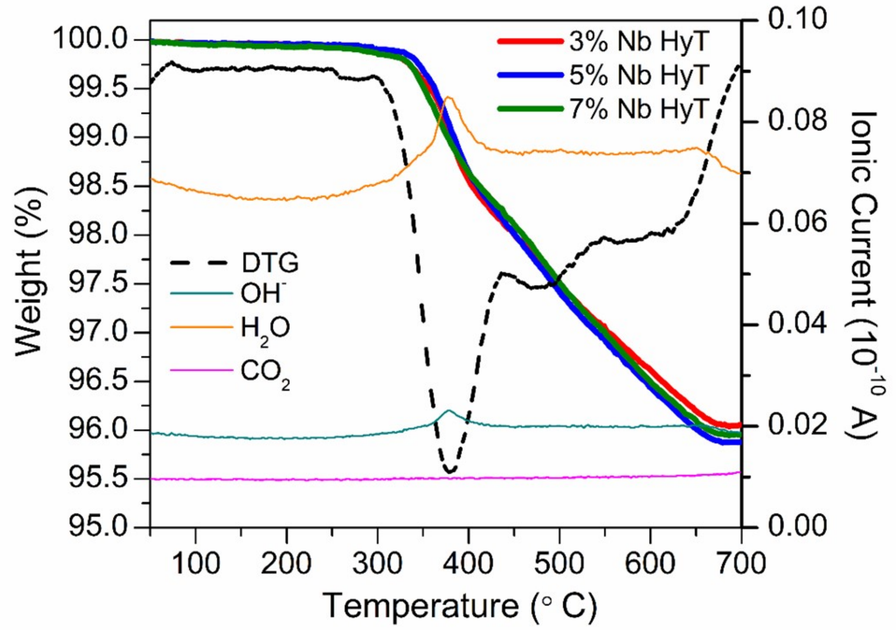

Figure S2. TG-MS spectrum of Nb-substituted HyT $LiVOPO_4$ under flowing N_2 at 10 °C/min. Solid red, blue, and green lines correspond to the TG curves for 3%, 5%, and 7% Nb-substituted HyT $LiVOPO_4$; dashed black line corresponds to the derivative of the TG curve; solid orange, dark cyan, and magenta lines correspond to the OH^-, H_2O, and CO_2 MS signals for 5% Nb-substituted HyT $LiVOPO_4$. The TGA curves reveal no significant differences between all samples, with almost identical onset temperatures of 325 °C and approximately 4% weight loss when heated to 700 °C (Figure 3). The experimental derivative TG (DTG) curve of the substituted samples illustrates that weight is mainly lost at 382, 481, and 581 °C. The most prominent DTG peak at 382 °C correlates with the evolution of H_2O and OH^- measured by the MS, similarly observed for the hydrogen vanadium phosphate (interchangeably known as H_2VOPO_4, $HVPO_4(OH)$, $VPO_4{\cdot}H_2O$).[1–4]

To calculate H/P molar ratios based on TG-MS measurements:

Assuming all weight lost from the starting material ($LiVOPO_4$) is in the form of H_2O,

$$4 \text{ wt. \% lost} = 4 \text{ g } H_2O \times \frac{1 \text{ mol H2O}}{18 \text{ g H2O}} \times \frac{2 \text{ mol H}}{1 \text{ mol H2O}} = 0.44 \text{ mol H}$$

$$96 \text{ wt. \% remaining} = 96 \text{ g } LiVOPO_4 \times \frac{1 \text{ mol LiVOPO4}}{169 \text{ g LiVOPO4}} \times \frac{1 \text{ mol P}}{1 \text{ mol LiVOPO4}} = 0.57 \text{ mol P}$$

$$\frac{0.44 \text{ mol H}}{0.57 \text{ mol P}} = 0.77 \text{ mol H/P}$$

To calculate H molar ratios based on CHNS analysis:

$$0.45 \text{ wt. \% lost} = 0.45 \text{ g H} \times \frac{1 \text{ mol H}}{1 \text{ g H}} = 0.45 \text{ mol H}$$

$$99.55 \text{ wt. \% remaining} = 99.55 \text{ g } LiVOPO_4 \times \frac{1 \text{ mol LiVOPO4}}{169 \text{ g LiVOPO4}} \times \frac{1 \text{ mol P}}{1 \text{ mol LiVOPO4}} = 0.59 \text{ mol P}$$

$$\frac{0.45 \text{ mol H}}{0.59 \text{ mol P}} = 0.76 \text{ mol H/P}$$

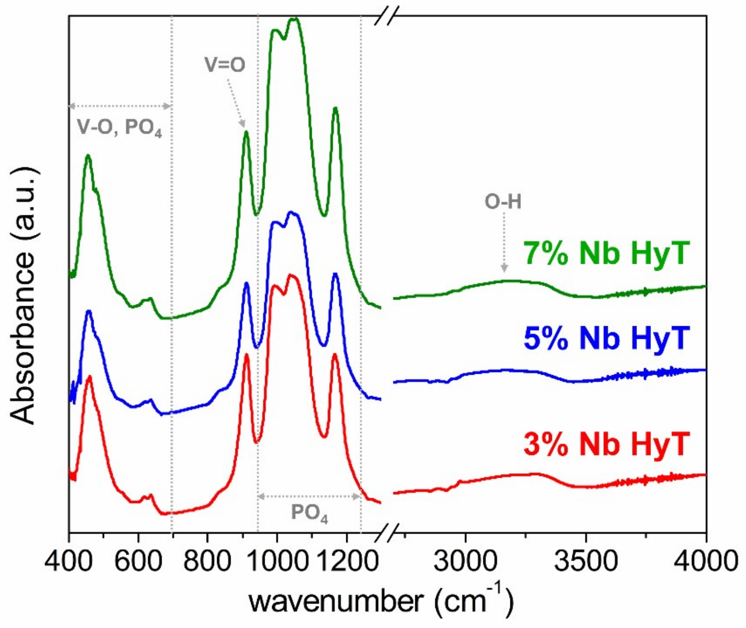

Figure S3. FT-IR spectra of Nb-substituted HyT $LiVOPO_4$. The bands between 420 - 605 cm^{-1} appear from the bending vibrations of P-O bonds and at 500 and 640 cm^{-1} from the bending and stretching vibrations of V-O bonds, respectively. A sharp band at 900 cm^{-1} is associated with the vanadyl bond, while the bands between 990 - 1150 cm^{-1} are related to the symmetric and asymmetric stretching vibrations of the phosphate ion.[5–7]

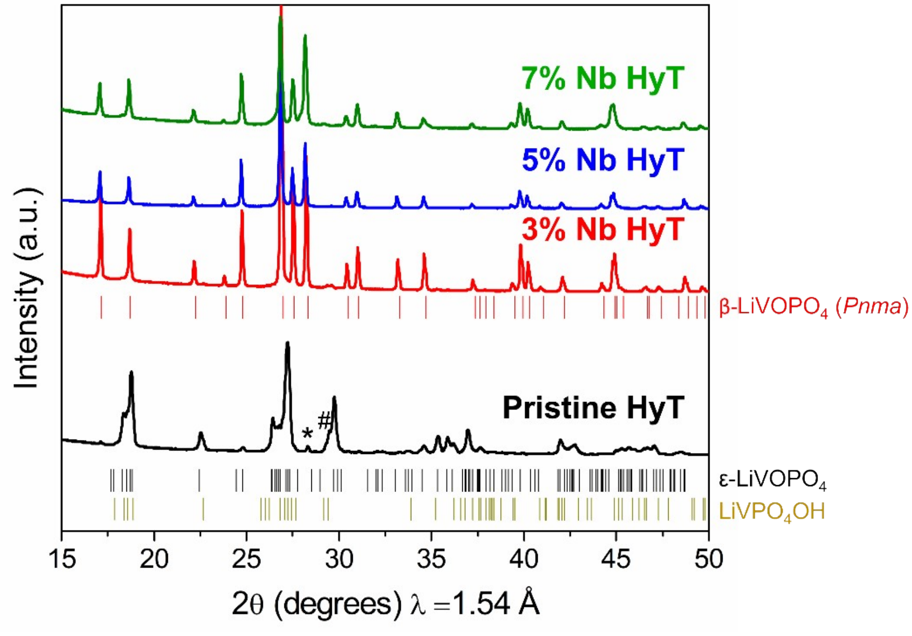

Figure S4. XRD patterns of $LiVOPO_4$ samples before and after the addition of the Nb precursor during hydrothermal synthesis. Without substitution, the hydrothermally-synthesized $LiVOPO_4$ (pristine HyT) yielded ε-$LiVOPO_4$ as the dominant phase with secondary phases of β-$LiVOPO_4$ and $LiVPO_4OH$, indicated by * and #, respectively. After the addition of Nb, the patterns of the substituted compounds resemble that of a different polymorph, β-$LiVOPO_4$, with a space group of *Pnma*. The substituent type was also shown to influence the phase stability of MWST-synthesized ε-$LiVOPO_4$, transforming to β-$LiVOPO_4$ after Nb substitution.[8]

Combined Rietveld refinements of the HRXRD and NPD patterns

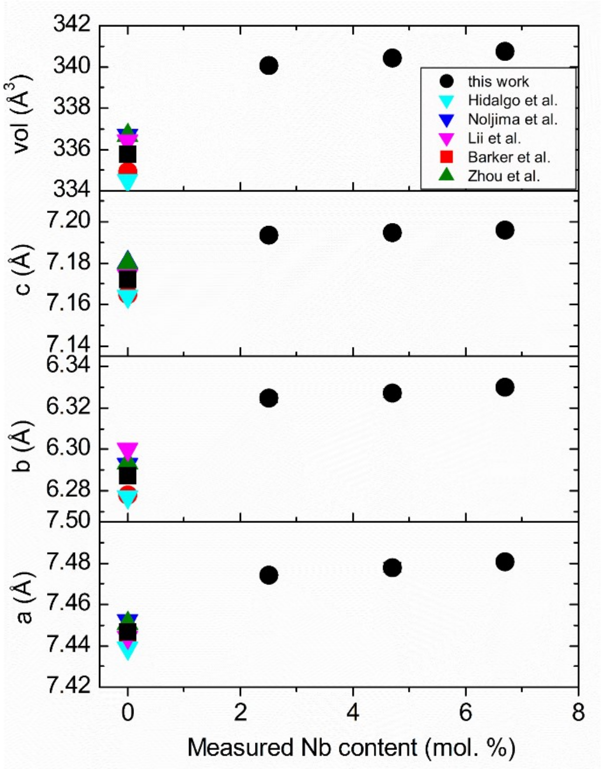

Figure S5. Lattice parameters of pristine HyTA and Nb-substituted HyT $LiVOPO_4$ as a function of ICP-OES-determined Nb concentration. Error bars are smaller than symbols. Colored symbols correspond to lattice parameters of β-$LiVOPO_4$ from the literature.[9–13]

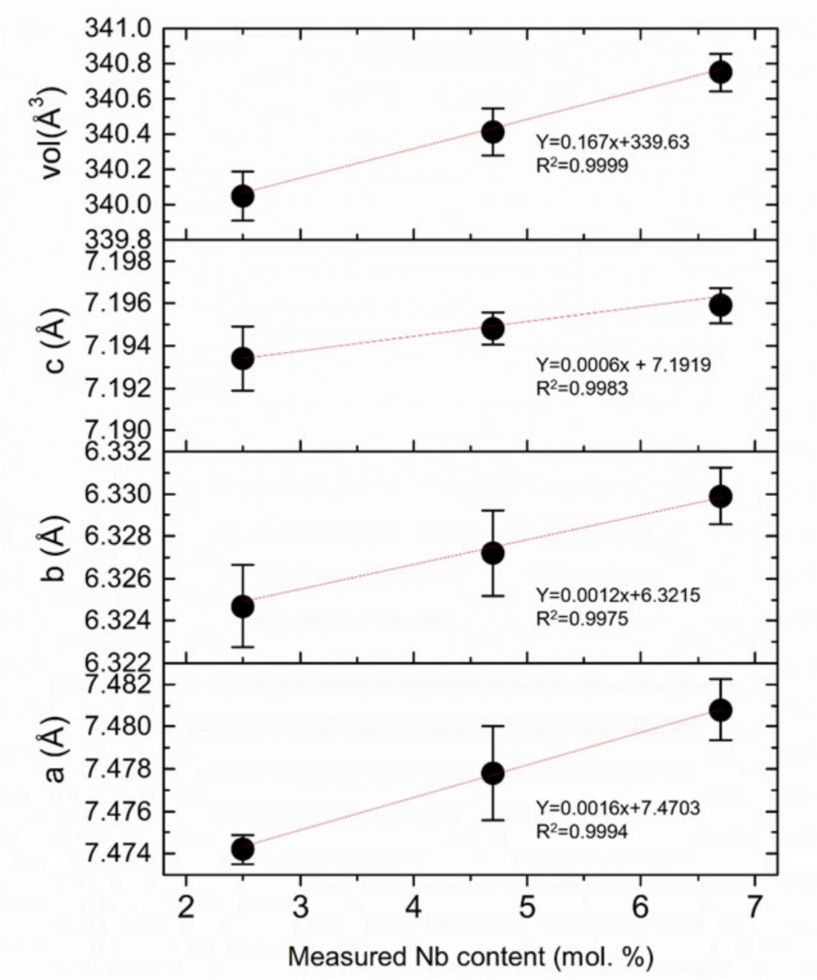

Figure S6. Lattice parameters of Nb-substituted HyT $LiVOPO_4$ as a function of ICP-OES-determined Nb concentration.

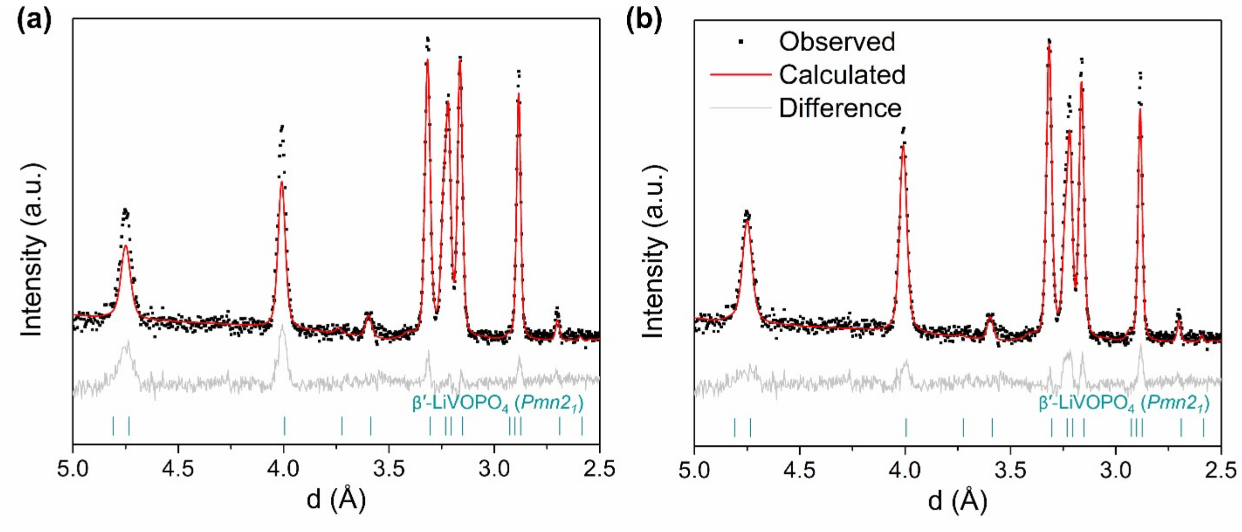

Figure S7. Rietveld refinement against the NPD patterns of 5% Nb-substituted HyT $LiVOPO_4$ using the structural model of β′-$LiVOPO_4$ (a) without and (b) with H. Black points correspond to the observed intensities, solid red lines correspond to the calculated intensities, and solid gray lines indicate the difference between these intensities.

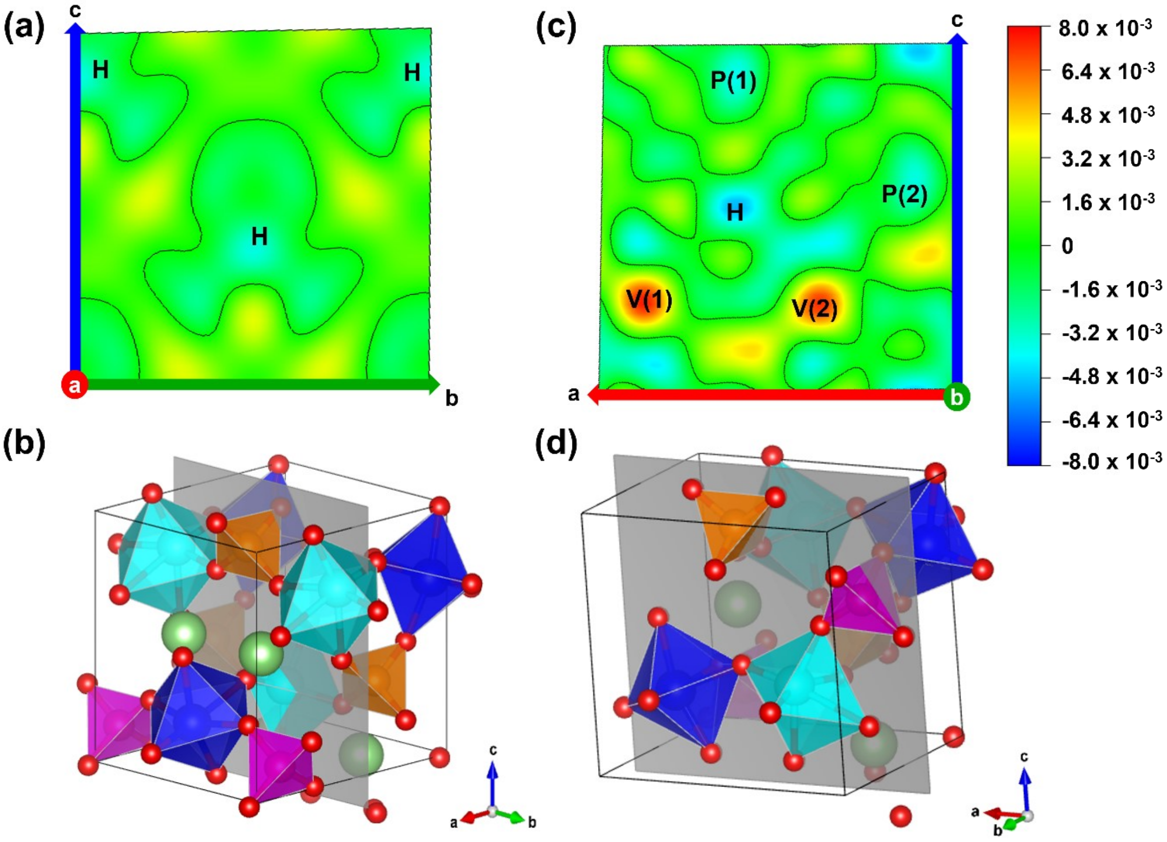

Figure S8. Fourier maps and corresponding structural model of 5% Nb-substituted HyT $LiVOPO_4$ for the (a-b) (200) plane (perpendicular to the V chain) and (c-d) (020) plane (along the V chain), using the structural model of β-$LiVOPO_4$ without the inclusion of H. Blue and red areas represent excess negative and positive nuclear scattering lengths, respectively. $V(1)O_6$ and $V(2)O_6$ octahedra in blue and teal, respectively; $P(1)O_4$ and $P(2)O_4$ tetrahedra in orange and magenta, respectively; Li atoms in green.

Analysis of the scattering power/lengths for the V and Li sites

Both HRXRD and NPD are used to determine the mixed occupancy of the Li and the V sites, which is not known *a priori* and cannot be obtained from other elemental analysis methods. It is possible that each site can be occupied simultaneously by Li, V, and Nb. Vacancies can also be formed based on the elemental analysis results. Therefore, the total site occupation should be determined by simultaneously refining the Li, V, and Nb occupancies for both the Li- and V-sites. However, this is an intractable problem even when both X-ray and neutron diffraction data are used for the refinement. (i.e., there are more unknowns than equations, so the system is underdetermined.)

In neutron diffraction, the site occupation is determined by the average nuclear scattering length density of the *i*th crystallographic site given by:

$$\bar{b}_i = \sum_k c_k b_k \quad \text{(S1)}$$

where the summation is over all nuclei occupying the site with occupancy of c_k and nuclear scattering length of b_k for nucleus k since the nuclear scattering length is effectively constant over the Q range of the diffraction measurement, the occupancy factor, c_k, cannot be unambiguously determined from the diffraction data alone for the mixed occupation by two or more elements. Additional information that defines the relationship between c_k is necessary to determine the mixed site occupation.

In X-ray diffraction, the site occupation is determined by the composite atomic form factor for the *i*th crystallographic site, which is given by:

$$f_i(Q) = \sum_k c_k f_k(Q) \quad \text{(S2)}$$

where f_k (Q) is the atomic form factor for atom k. Although the Q dependence of the atomic form factor, f (Q), in X-ray diffraction can be used in principle to distinguish different elements, the difference in the Q dependence between different elements is too small to be distinguished in practice. Therefore, neither XRD nor NPD alone, without any other structural or compositional information, can determine the mixed site occupancy when more than two different species (including vacancy) occupy the same crystallographic site. Given this inherent limitation, the structure models we tested only consider the mixed occupation of two elements, i.e., Li and V, Li and Nb, or V and Nb. Note that vacancy concentration is implicitly incorporated in these structural models because $\sum_k c_k$ (k= Li, V, or Nb) is not constrained to unity.

To determine whether Nb substitutes in the crystal structure, we refined the averaged scattering length (power) of the Li- and V-sites for the neutron (X-ray) diffraction data. The structure model only considers the occupation of Li- and V-sites by Li and V, respectively, which serve as proxy atoms to approximate the average scattering power of the Li- and V-sites. For the HRXRD refinement, peaks below 12.6 ° = 2θ were excluded to mitigate the uncertainty of refined atomic site occupation due to the ill-defined atomic scattering factor at low Q for ionic species in solids.[14] The higher symmetry structure model (*Pnma*) was adopted for the Rietveld refinement, where all structural parameters were simultaneously refined. The refined average scattering power for Li-site (V-site) is determined by $c_{Li}f_{Li}$ ($c_V f_V$). The refined average scattering power (at Q = 0) for both the Li- and V-sites increases with increasing Nb concentration (Figure S9). It is noted that the $\bar{f}_{4b}(Q = 0)$ corresponds to more than unity occupation by Li, which suggests the mixed occupation by a heavier element (i.e., Nb or V or both). $\bar{f}_{4c}(Q = 0)$ corresponds to less than unity occupation by V, which suggests the presence of vacancies.

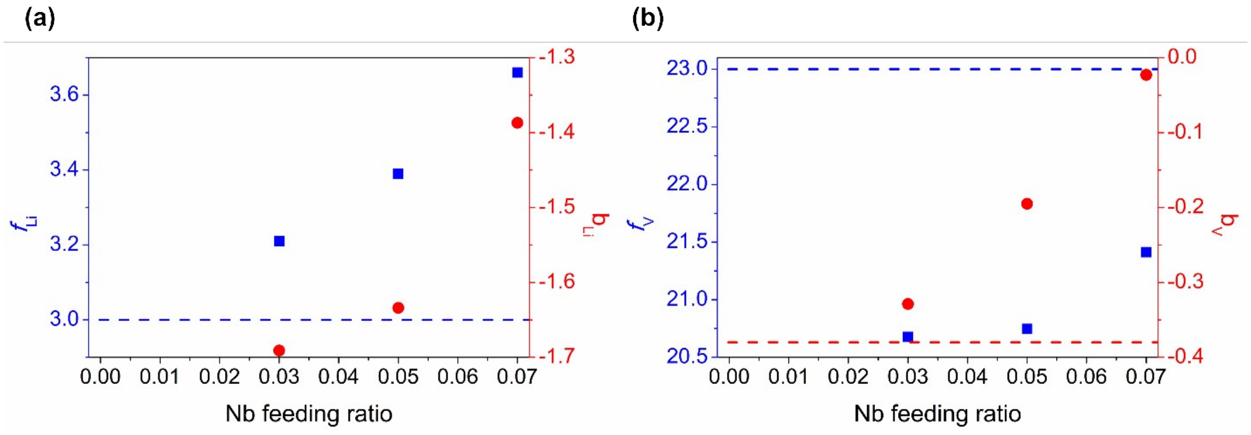

Figure S9. Refined average scattering power at Q = 0 (length) for (a) the Li-site (*4b*) and (b) the V-site (*4c*). Dashed blue (red) lines correspond to the scattering power (length) of full occupation by Li or V. The scattering length of Li (-1.9 fm) is out of the range.

Investigation of co-occupation by Li, V, Nb, and vacancies in the V and Li sites

The same structure model (*Pnma*), used in the HRXRD patterns analysis, was adopted for the NPD data. All structural parameters, except the atomic coordinates and the ADP for the V site, were simultaneously refined. Values obtained from the HRXRD refinement were used for the atomic coordinates and the ADP for the V site to overcome the uncertainty due to the small scattering length of V in NPD. The refined average scatterings lengths for both the V-site ($\bar{b}_{4c}$) and the Li-site ($\bar{b}_{4b}$) increase with increasing Nb feeding ratio (Figure S9). Since the scattering lengths for both V and Li are negative, this increase can be explained by either the increased vacancy concentration or the co-occupation by Nb (the only cation with a positive scattering length in the sample) or both.

The refined average scattering power (length) corresponds to a *surface* in the three-dimensional compositional space defined by c_{Li}, c_V, and c_{Nb}, which are the site occupancies of Li, V, and Nb, respectively. Since each unique composition (c_{Li}, c_V, c_{Nb}) on this surface corresponds to the same average scattering power (length), it is impossible to obtain the actual Li, V, and Nb composition for each crystallographic site based only on the refinement against the X-ray (neutron) diffraction data. Joint refinement, using both the HRXRD and NPD data, reduces the *surface* to a *line* in the (c_{Li}, c_V, c_{Nb}) space, yet a unique solution is still not possible without imposing other constraints to reduce the *line* to a *point* in the compositional space. Therefore, we considered different mixed-site occupation models to introduce additional constraints to allow for the evaluation of their plausibility.

For the V-site, each of the following constraints was considered:

$$c_V + c_{Li} + c_{Nb} = 1 \quad \text{(S3)}$$

$$c_V + c_{Li} + c_{vac} = 1 \quad \text{(S4)}$$

$$c_V + c_{vac} + c_{Nb} = 1 \quad \text{(S5)}$$

The additional constraint reduces the refined $\bar{b}_{4c}$ or $\bar{f}_{4c}$ to a line in Figure S10a-c and Figure S10d-f, respectively, in the two-dimensional compositional space for the 5% Nb-substituted sample. $\bar{b}_{4c}$ is represented by the white lines in Figure S10a-c and the green line in Figure S10g-i; $\bar{f}_{4c}$ is represented by the white lines in Figure S10d-f and the red line in Figure S10g-i. Only the plausible compositional range ($0.7 < c_V < 1$, $0 < c_{Li} < 0.3$, $0 < c_{Nb} < 0.3$) is shown in the plot. A unique composition can be identified at the intersection between the lines corresponding to $\bar{b}_{4c}$ and $\bar{f}_{4c}$

(yellow dots in Figure S10g-i). It is evident that the co-occupation of the V-site (*4c*) by Li and vacancy cannot account for the refined $\bar{b}_{4c}$ and $\bar{f}_{4c}$ simultaneously (because of the lack of an intersection between the lines for $\bar{b}_{4c}$ and $\bar{f}_{4c}$ in Figure S10h), and the co-occupation by Nb is necessary to explain both the HRXRD and NPD data. Therefore, the diffraction data demonstrates the substitution of Nb in V-site (*4c*). The same conclusion also holds for the 3% and 7% Nb-substituted samples.

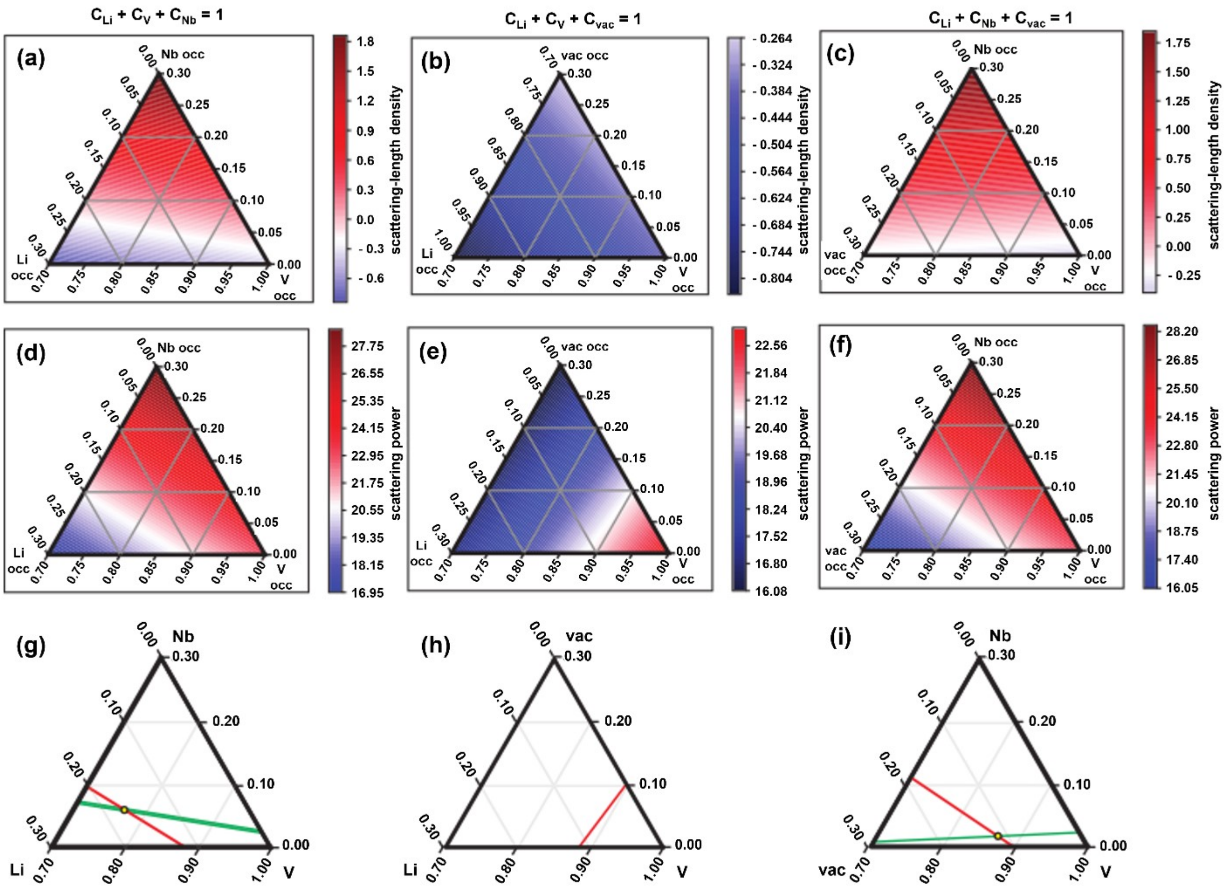

Figure S10. (a-c) Scattering length and (d-f) scattering power for the V-site as a function of the mixed site occupation, white lines correspond to the refined values of scattering length/power. (g-i) Compositions corresponding to the refined average scattering power (red line) and scattering length (green line).

For the Li-site (*4b*) occupation, each of the following constraints was considered:

$$c_{Li} + c_V + c_{Nb} = 1 \qquad (S6)$$

$$c_{Li} + c_V + c_{vac} = 1 \qquad (S7)$$

$$c_{Li} + c_{vac} + c_{Nb} = 1 \qquad (S8)$$

Following the same analysis performed for the V-site (*4c*) site, the refined $\bar{b}_{4b}$ and $\bar{f}_{4b}$ in the two-dimensional compositional space are plotted in Figure S11 for the 5% Nb-substituted sample. It is concluded that vacancies and co-occupation by V and/or Nb are necessary to explain both the HRXRD and NPD data.

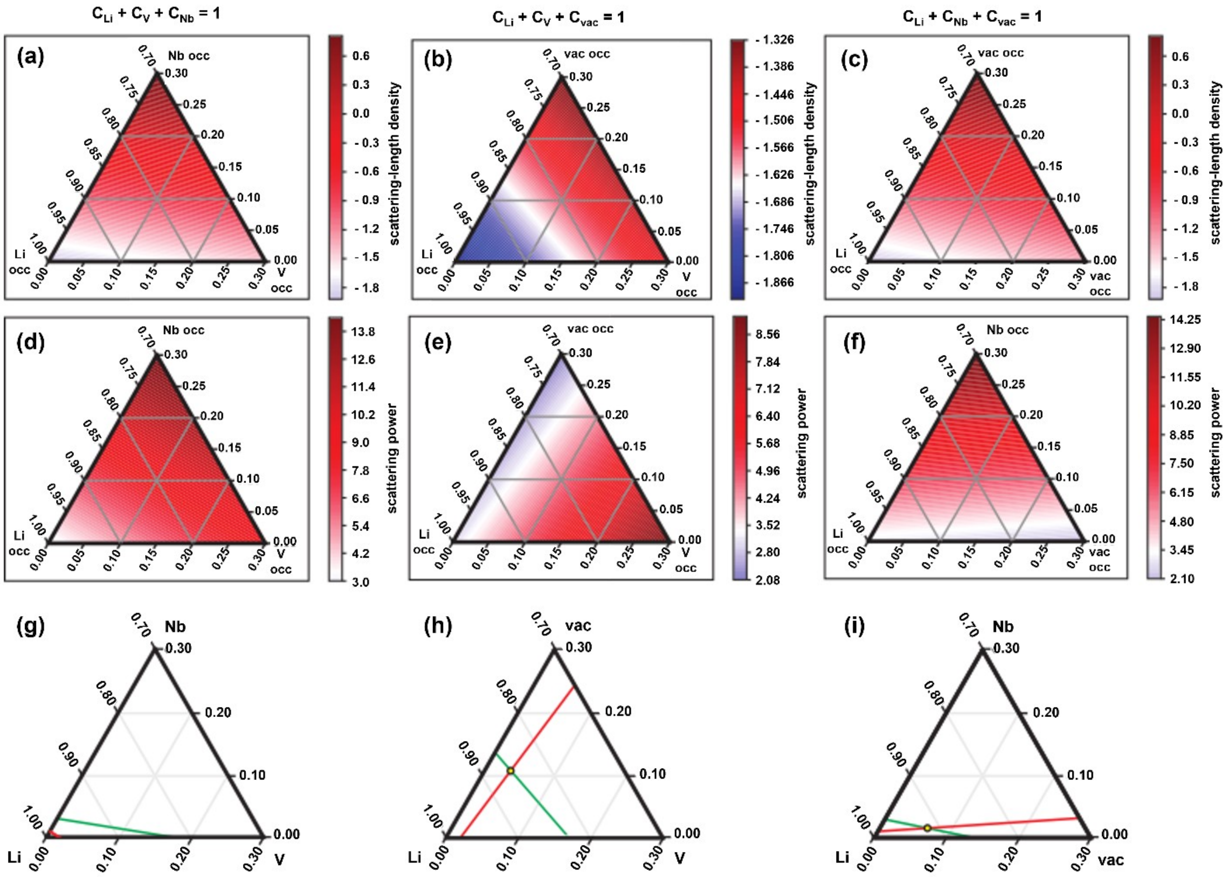

Figure S11. (a-c) Scattering length and (d-f) scattering power for the Li-site as a function of the mixed site occupation, white lines correspond to the refined values of scattering length/power.

(g-i) Compositions corresponding to the refined average scattering power (red line) and scattering length (green line).

Table S2. Structural parameters obtained from combined Rietveld refinement against the HRXRD and NPD patterns of 3% Nb-substituted HyT $LiVOPO_4$.

3% Nb-substituted HyT

SG = *Pmn2₁*	*a* = 7.4742(1) Å	R_{wp} = 2.09 %
β′-$LiVOPO_4$ = 96.99 %	*b* = 6.3247(6) Å	R_{exp} = 3.08 %
$LiVPO_4OH$ = 3.01 %	*c* = 7.1934(9) Å	
	Vol = 340.048(7) Å^3	

Atoms	**x**	**y**	**z**	**Occupancy**	**Wyckoff position**	**ADP (Å^2)**
V(1)	0.0852(6)	0	-0.278(1)	0.91(1)	2a	0.70(3)
Nb(1)	0.0852(6)	0	-0.278(1)	0.017(5)	2a	0.70(3)
V(2)	0.5743(6)	0	-0.223(1)	0.94(1)	2a	0.70(3)
Nb(2)	0.5743(6)	0	-0.223(1)	0.000(5)	2a	0.70(3)
Li(1)	0.7507(4)	0.7260(4)	0.5087(1)	0.911(7)	4b	0.53(3)
V(3)	0.7507(4)	0.7260(4)	0.5087(1)	0.014(2)	4b	0.70(3)
P(1)	0.3795(2)	0	0.6274(3)	1	2a	0.391(5)
P(2)	0.8748(3)	0	0.8736(2)	1	2a	0.391(5)
O(1)	0.0366(2)	0	0.0054(2)	1	2a	0.815(3)
O(2)	0.5536(2)	0	0.5112(2)	1	2a	0.815(3)
O(3)	0.1270(2)	0.6961(3)	0.2462(2)	1	4b	0.815(3)
O(4)	0.6188(2)	0.3058(3)	0.2566(2)	1	4b	0.815(3)
O(5)*	0.8678(3)	0	0.3619(2)	1	2a	0.815(3)
O(6)*	0.3715(3)	0	0.1624(2)	1	2a	0.815(3)
O(7)	0.2116(3)	0	0.5075(3)	1	2a	0.815(3)
O(8)	0.7042(3)	0	0.0092(3)	1	2a	0.815(3)
H(1)	0.009(2)	0.371(2)	0.074(2)	0.113(4)	4b	1
H(2)	0.686(2)	0.574(2)	0.490(2)	0.106(4)	4b	1

*The oxygens in the closest proximity to H

Table S3. Structural parameters obtained from combined Rietveld refinement against the HRXRD and NPD patterns of 7% Nb-substituted HyT $LiVOPO_4$.

7% Nb-substituted HyT

SG = *$Pmn2_1$*		a = 7.4808(1) Å		R_{wp} = 4.33 %		
β′-$LiVOPO_4$ = 97.42 %		b = 6.3299(1) Å		R_{exp} = 2.37 %		
$LiVPO_4OH$ = 2.55 %		c = 7.1959(1) Å				
		Vol = 340.75(1) $Å^3$				
Atoms	**x**	**y**	**z**	**Occupancy**	**Wyckoff position**	**ADP ($Å^2$)**
V(1)	0.0877(1)	0	0.2848(1)	0.83(2)	2a	0.726(9)
Nb(1)	0.0877(1)	0	0.2848(1)	0.07(1)	2a	0.726(9)
V(2)	0.5745(1)	0	0.2327(1)	0.96(2)	2a	0.726(9)
Nb(2)	0.5745(1)	0	0.2327(1)	0.00(1)	2a	0.726(9)
Li(1)	0.754(1)	0.747(1)	0.501(1)	0.81(2)	4b	1.27(7)
V(3)	0.754(1)	0.747(1)	0.501(1)	0.038(2)	4b	0.726(9)
P(1)	0.3772(3)	0	0.6423(3)	1	2a	0.593(8)
P(2)	0.8760(2)	0	0.8888(3)	1	2a	0.593(8)
O(1)	0.0431(4)	0	0.0140(6)	1	2a	0.790(7)
O(2)	0.5456(4)	0	0.5174(5)	1	2a	0.790(7)
O(3)	0.1244(3)	0.6966(4)	0.2592(4)	1	4b	0.790(7)
O(4)	0.6208(3)	0.3056(4)	0.2699(4)	1	4b	0.790(7)
O(5)*	0.8750(4)	0	0.3554(5)	1	2a	0.790(7)
O(6)*	0.3671(5)	0	0.1578(5)	1	2a	0.790(7)
O(7)	0.2191(3)	0	0.5155(4)	1	2a	0.790(7)
O(8)	0.6964(3)	0	0.0011(4)	1	2a	0.790(7)
H(1)	0.011(3)	0.395(3)	0.088(3)	0.217(7)	4b	1
H(2)	0.701(3)	0.601(4)	0.452(4)	0.16(1)	4b	1

*The oxygens in the closest proximity to H

Table S4. Elemental composition of Nb-substituted HyT LiVOPO$_4$ determined by Rietveld refinement of the combined diffraction results (NX) and the difference from the ICP-OES-determined values.

Sample	**$\mathrm{Li_{NX}}$**	**$\lvert \mathrm{Li_{diff}} \rvert$**	**$\mathrm{V_{NX}}$**	**$\lvert \mathrm{V_{diff}} \rvert$**	**$\mathrm{Nb_{NX}}$**	**$\lvert \mathrm{Nb_{diff}} \rvert$**
3% Nb	0.884(0)	0.052(0)	0.94(0)	0.02(0)	0.008(5)	0.017(1)
5% Nb	0.88(1)	0.09(3)	0.92(4)	0.00(9)	0.02(5)	0.02(2)
7% Nb	0.79(0)	0.04(0)	0.93(3)	0.01(4)	0.03(1)	0.03(1)

Table S5. Bond lengths in coordination with the crystallographically distinct P and V sites obtained from combined Rietveld refinement of Nb-substituted HyT LiVOPO$_4$.

Sample		**P(1)O$_4$ bond lengths (Å)**					
		O(7)	**O(4)**	**O(4)**	**O(2)**		
3% Nb	**P(1)**	1.523(3)	1.540(2)	1.540(2)	1.547(2)		
5% Nb		1.513(3)	1.521(3)	1.521(3)	1.571(3)		
7% Nb		1.493(3)	1.535(3)	1.535(3)	1.547(4)		
		P(2)O$_4$ bond length (Å)					
		O(8)	O(1)	O(3)	O(3)		
3% Nb	**P(2)**	1.529(3)	1.537(2)	1.542(2)	1.542(2)		
5% Nb		1.517(3)	1.536(3)	1.568(3)	1.568(3)		
7% Nb		1.559(3)	1.540(4)	1.554(3)	1.554(3)		
		V(1)O$_6$ bond length (Å)					
		O(5)*	O(7)	O(3)	O(3)	O(1)	O(6)*
3% Nb	**V(1)**	1.734(5)	1.904(7)	1.961(2)	1.961(2)	1.993(8)	2.295(5)
5% Nb		1.709(3)	1.901(3)	1.958(3)	1.958(3)	1.996(3)	2.273(3)
7% Nb		1.669(3)	1.929(3)	1.947(3)	1.947(3)	1.976(4)	2.280(4)
		V(2)O$_6$ bond length (Å)					
		O(6)*	O(8)	O(4)	O(4)	O(2)	O(5)*
3% Nb	**V(2)**	1.578(5)	1.935(8)	1.977(2)	1.977(2)	2.075(8)	2.410(5)
5% Nb		1.609(3)	1.942(3)	1.978(3)	1.978(3)	2.069(3)	2.421(3)
7% Nb		1.642(4)	1.913(3)	1.982(3)	1.982(3)	2.059(4)	2.415(3)

*The oxygens in the closest proximity to H

X-ray PDF

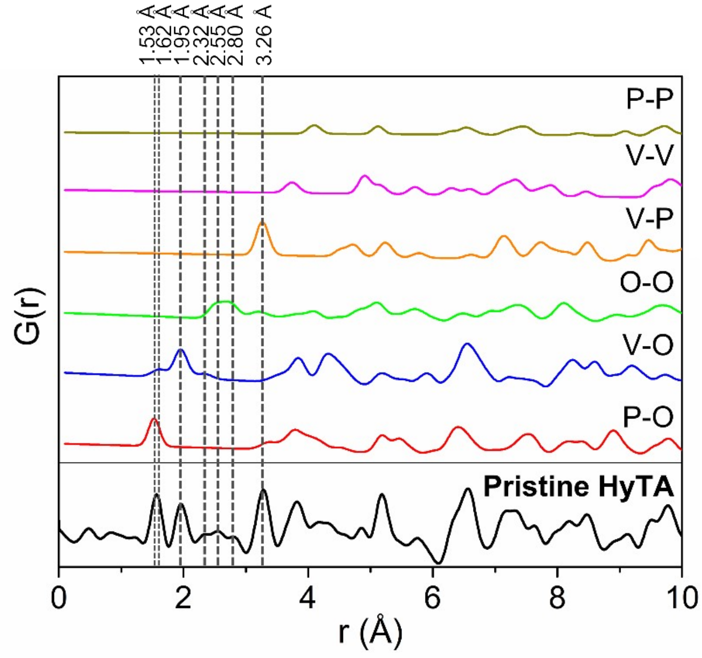

Figure S12. Characteristic atom-atom pair analysis of the reference sample, pristine HyTA. The first six peaks are associated with the bonds of (1) P-O and V=O, (2) V-O_{eq}, (3) long V-O, (4) and (5) O-O, and (6) V-P.

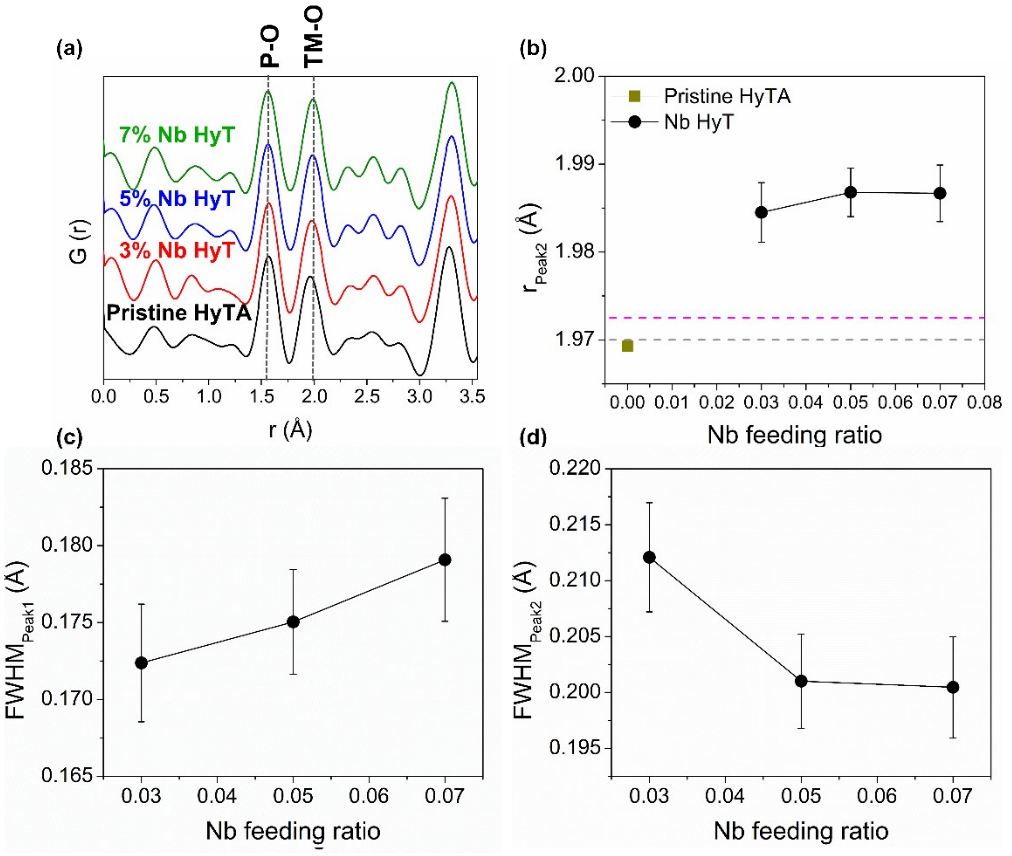

Figure S13. (a) Total PDF patterns of pristine HyTA and Nb-substituted HyT $LiVOPO_4$ with the corresponding characteristic atom-atom pairs of the first two peaks. (b) The interatomic distances of Peak 2 and the full width at half maximum (FWHM) of Peaks (c) 1 and (d) 2 are plotted as a function of Nb feeding ratio. Dashed lines correspond to the equatorial V-O bond lengths of V^{4+} compounds, β-$LiVOPO_4$ (gray) and VO_2 (pink) from the literature.[11,15] The first two peaks can be assigned to the P-O (1.57 Å) and TM-O_{eq} (1.99 Å) bonds, respectively, based on the calculated partial PDFs for β-$LiVOPO_4$. Single peak fitting was performed to extract the average bond lengths and the FWHM. The average P-O and TM-O_{eq} bonds remain unchanged with increasing substitution, the TM-O_{eq} bond increasing only marginally from 1.985 Å for the 3% to 1.987 Å for the 7% Nb substituted samples.

Magnetic susceptibility

Table S6. Magnetic parameters obtained by the Curie-Weiss Law for Nb-substituted HyT $LiVOPO_4$.

Sample	χ_0, 10^{-4} (emu)	Θ (K)	C (emu/K)
3% Nb	-8	-20.7(1)	0.373(1)
5% Nb	4.4	-15.8(1)	0.349(1)
7% Nb	-25.6	-13.7(1)	0.348(1)

To calculate the normalized Curie constant to account for transition metal deficiency determined by ICP-OES (C_{ICP}):

$\chi = \chi_0 + C/\Theta$

C_{ICP}= C/total TM determined from ICP-OES

To calculate effective magnetic moment (μ):

$C_{ICP} = N_A\, \mu_{eff}^2/3k_B = 1/8\mu_{ICP}^2$

To calculate amounts of V^{4+} and V^{3+}:

$\mu_{eff} = g\sqrt{S(S+1)}$ where g = 2

For V^{4+} → d^1, S=1/2 then = 1.73 μB

For V^{3+} → d^2, S=1 then = 2.83 μB

$\mu_{ICP}^2 = x(1.73^2) + 1 - x(2.83^2)$, where x = fraction of V^{4+}

Concentration of V^{4+} = x * total amount of V determined by ICP-OES

Concentration of V^{3+} = (1-x) * total amount of V determined by ICP-OES

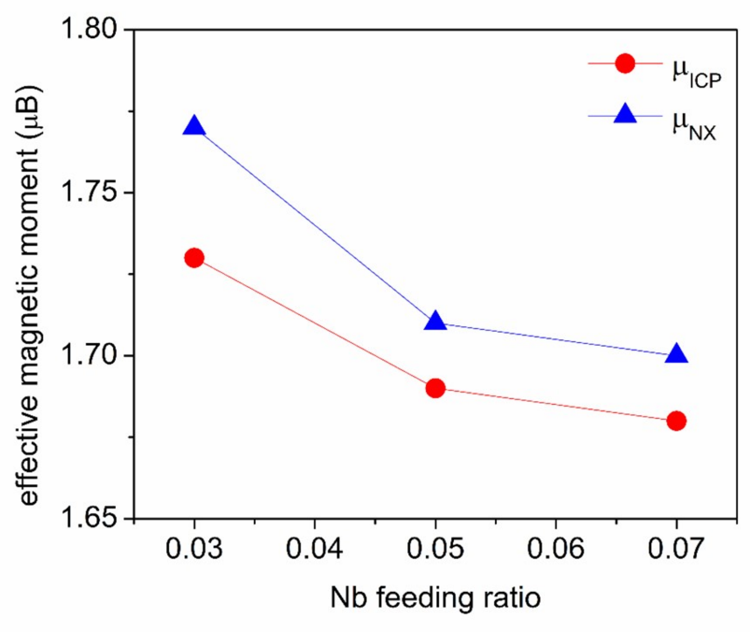

Figure S14. Comparison of the effective magnetic moments calculated based on the TM content determined by ICP-OES (μ_{ICP}) and combined HRXRD and NPD refinement (μ_{NX}).

Table S7. Curie constants and the effective magnetic moments of Nb-substituted HyT $LiVOPO_4$ calculated based on TM feeding ratios used in the synthesis (μ_{theo}) and the total TM content from ICP-OES (μ_{ICP}) and combined Rietveld refinement results (μ_{NX}). The ratios of V^{3+}/P and V^{4+}/P calculated based on μ_{ICP}.

Sample	**C_{exp} (emu/K)**	**C_{ICP} (emu/K mol)**	**C_{NX} (emu/K mol)**	**μ_{theo} (μB)**	**μ_{ICP} (μB)**	**μ_{NX} (μB)**	**Nb^{5+}/P_{ICP}**	**V^{4+}/P_{calc}**	**V^{3+}/P_{calc}**
3% Nb	0.373(1)	0.376(1)	0.393(1)	1.71	1.73	1.77	0.0248(2)	0.950(3)	0.018(0)
5% Nb	0.349(1)	0.356(1)	0.367(1)	1.69	1.69	1.71	0.0468(9)	0.934(0)	-0.001(0)
7% Nb	0.348(1)	0.353(1)	0.360(1)	1.67	1.68	1.70	0.0672(1)	0.912(0)	0.007(4)

Charge compensation mechanism of Nb-substituted $LiVOPO_4$

Table S8. Summary of cationic charges and molar ratio values, all normalized to P, along with the H analysis of Nb-substituted HyT $LiVOPO_4$. The total cationic charge ($Tot_{cat.chg}$,) is calculated based on ICP-OES-determined values, H^+ is calculated to equal to the cationic deficiencies in the substituted materials; $\Delta_{Htot-H+}$ is the difference between CHNS-determined H (H_{tot}) and H^+.

	Measured					**Calculated**		
Method	**ICP**			**CHNS**	**NX**			
Sample	**Li^+/P**	**V^{4+}/P**	**Nb^{5+}/P**	**H/P**	**H/P**	**$Tot_{cat.chg}$**	**H^+**	**$\Delta_{Htot-H+}$**
3% Nb	0.832(2)	0.968(4)	0.0248(2)	0.777(3)	0.219(0)	4.830	0.170	0.61
5% Nb	0.786(2)	0.933(2)	0.0468(9)	0.827(3)	0.341(0)	4.754	0.246	0.58
7% Nb	0.753(3)	0.919(3)	0.0672(1)	0.794(3)	0.37(7)	4.767	0.232	0.56

SEM after ball-milling

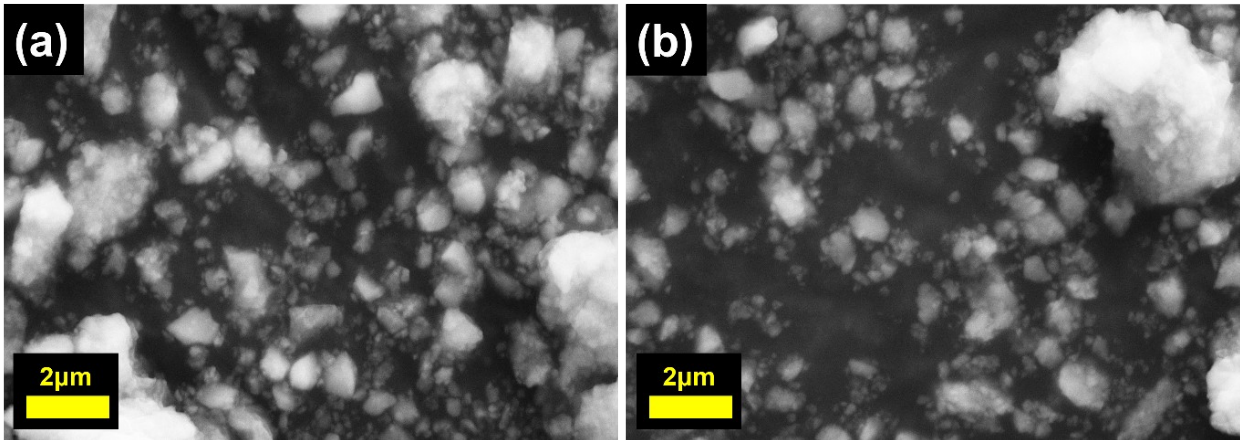

Figure S15. SEM images of (a) pristine HyTA and (b) Nb-substituted HyT $LiVOPO_4$ after high-energy ball-milling with graphene nanoplatelets.

GITT measurements

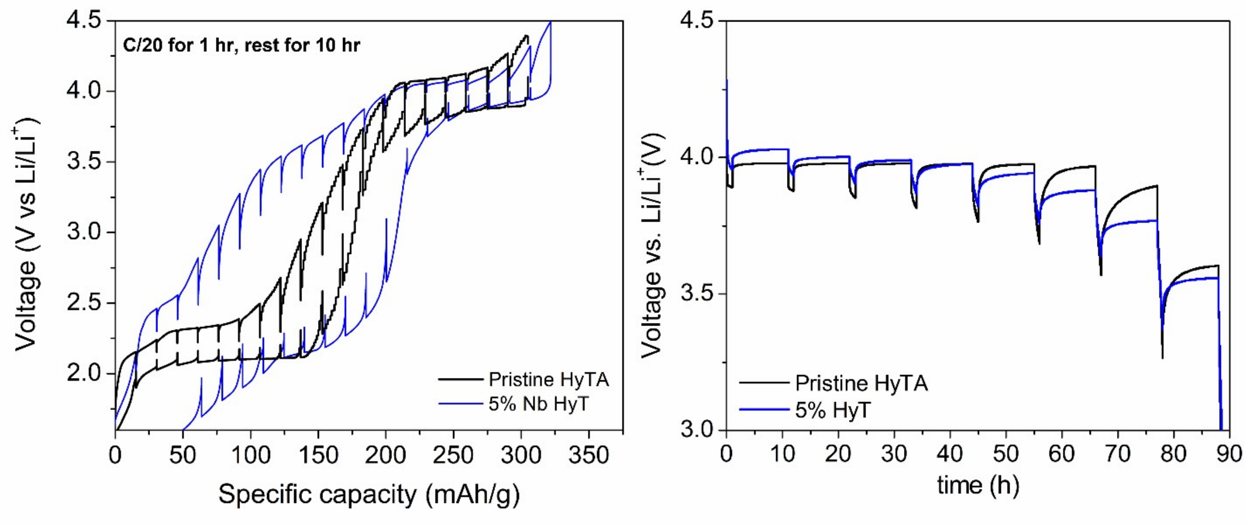

Figure S16. GITT measurements of pristine HyTA and 5% Nb-substituted HyT $LiVOPO_4$ conducted at a current rate of C/20 for 1 hour, followed by a 10-hour rest period, showing the (a) capacity−voltage profiles within 1.6 – 4.5 V and (b) time−voltage profiles within the high-voltage (3.0 – 4.5 V) region.

Ex-situ XAS

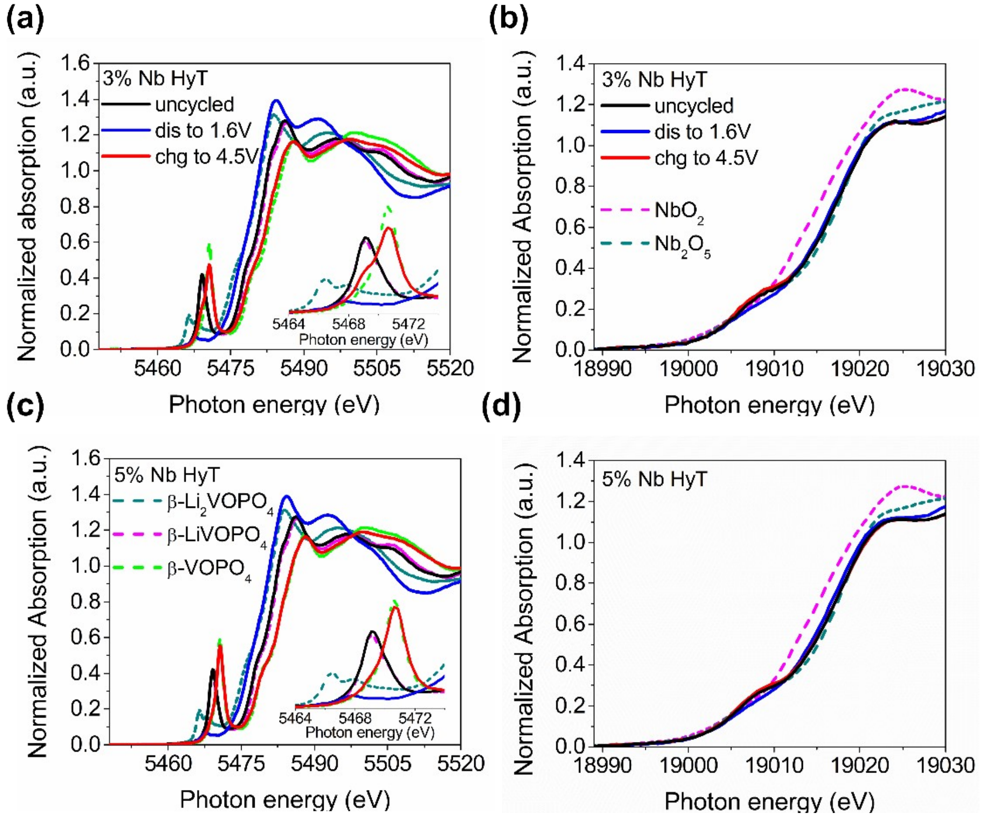

Figure S17. XAS spectra at the (left) V and (right) Nb K-edges of electrochemically charged and discharged (a-b) 3% and (c-d) 5% Nb-substituted HyT $LiVOPO_4$. The inset shows an enlarged pre-edge region.

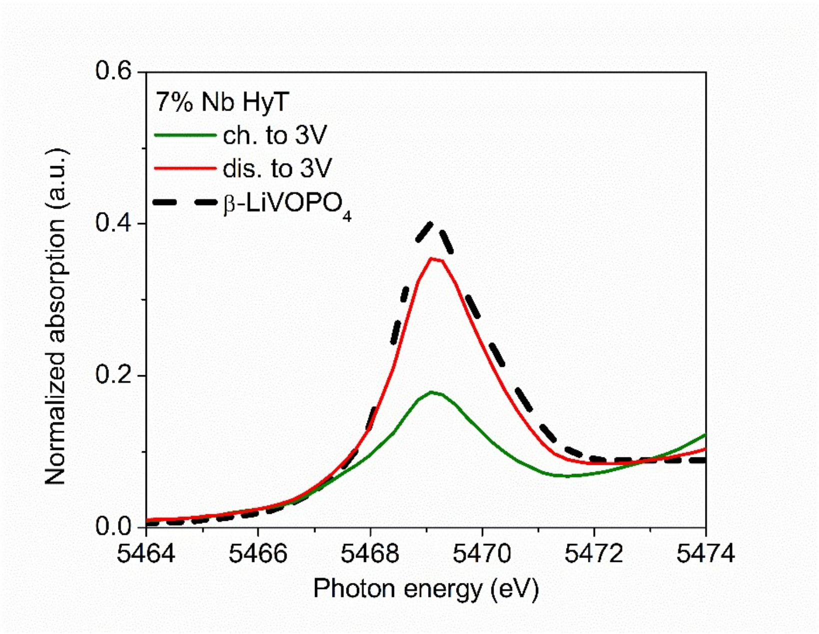

Figure S18. XAS spectra at the V K-edge of 7% Nb-substituted HyT LiVOPO$_4$ illustrate the discrepancy in the pre-edge feature between the samples charged and discharged to 3 V.

Ex-situ X-ray PDF

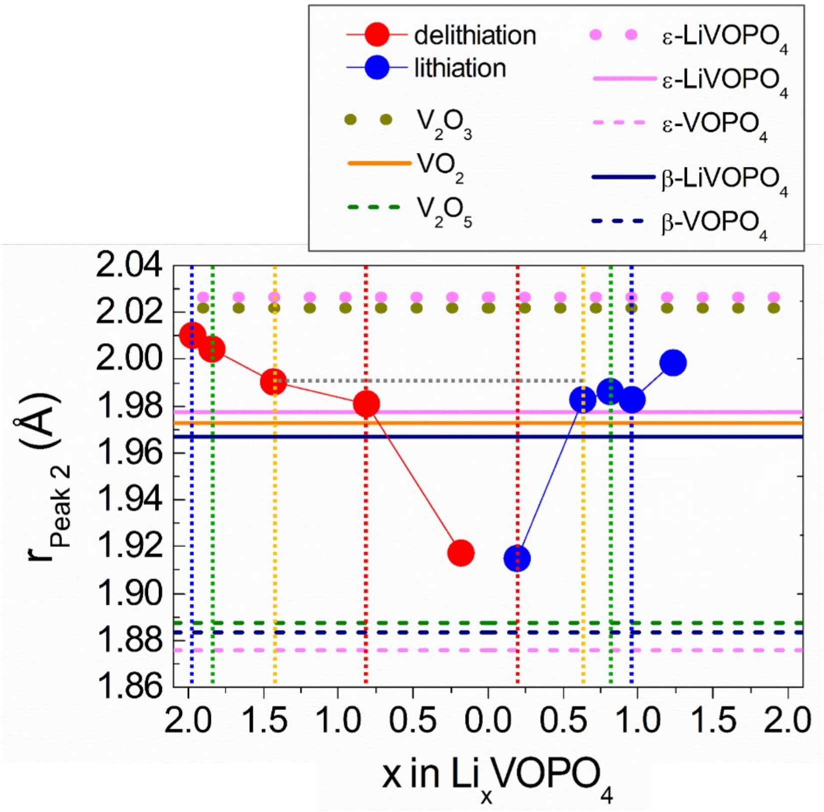

Figure S19. The interatomic distances of Peak 2 as a function of Li content for 7% Nb-substituted HyT $LiVOPO_4$ during the electrochemical process of 1.6 – 4.5 V. Dashed vertical lines of matching colors correspond to samples recovered at the same potentials; dashed horizontal gray line shows the discrepancy between samples charged and discharged to 3 V; colored horizontal lines correspond to the V-O bond lengths of V^{5+}(dashed), V^{4+}(solid), and V^{3+}(dotted) compounds from the literature.[15–19]

References

1) Song, Y.; Zavalij, P. Y.; Whittingham, M. S. ε-$VOPO_4$: Electrochemical Synthesis and Enhanced Cathode Behavior. *J. Electrochem. Soc.* **2005**, *152* (4), A721–A728.
2) Boivin, E.; Chotard, J.-N.; Ménétrier, M.; Bourgeois, L.; Bamine, T.; Carlier, D.; Fauth, F.; Suard, E.; Masquelier, C.; Croguennec, L. Structural and Electrochemical Studies of a New Tavorite Composition: $LiVPO_4OH$. *J. Mater. Chem. A* **2016**, *4* (28), 11030–11045.
3) Lim, S. C.; Vaughey, J. T.; Harrison, W. T. A.; Dussak, L. L.; Jacobson, A. J.; Johnson, J. W. Redox Transformations of Simple Vanadium Phosphates: The Synthesis of ε-$VOPO_4$. *Solid State Ion.* **1996**, *84*, 219–226.
4) Vaughey, J. T.; Harrison, W. T. A.; Jacobson, A. J.; Goshorn, D. P.; Johnson, J. W. Synthesis, Structure, and Properties of Two New Vanadium (III) Phosphates: $VPO_4 \cdot H_2O$ and $V_{1.23}(PO_4)(OH)_{0.69}(H_2O)_{0.31} \cdot 0.33H_2O$. *Inorg. Chem.* **1994**, *33* (11), 2481–2487.
5) Harrison, K. L.; Manthiram, A. Microwave-Assisted Solvothermal Synthesis and Characterization of Various Polymorphs of $LiVOPO_4$. *Chem. Mater.* 2013, *25* (9), 1751–1760.
6) Yang, Y.; Fang, H.; Zheng, J.; Li, L.; Li, G.; Yan, G. Towards the Understanding of Poor Electrochemical Activity of Triclinic $LiVOPO_4$: Experimental Characterization and Theoretical Investigations. *Solid State Sci.* **2008**, *10* (10), 1292–1298.
7) Wang, L.; Yang, L.; Gong, L.; Jiang, X.; Yuan, K.; Hu, Z. Synthesis of $LiVOPO_4$ for Cathode Materials by Coordination and Microwave Sintering. *Electrochimica Acta* **2011**, *56* (20), 6906–6911.
8) Kaplan, C.; Hidalgo, M. F. V.; Zuba, M. J.; Chernova, N. A.; Piper, L. F. J.; Whittingham, M. S. Microwave-Assisted Solvothermal Synthesis of LiV_yM_{1-y} OPO_4 (M = Mn, Cr, Ti, Zr, Nb, Mo, W) Cathode Materials for Lithium-Ion Batteries. *J. Mater. Chem. A* **2021**, *9* (11), 6933–6944.
9) Hidalgo, M. F. V.; Lin, Y.-C.; Grenier, A.; Xiao, D.; Rana, J.; Tran, R.; Xin, H.; Zuba, M.; Donohue, J.; Omenya, F. O.; Chu, I.-H.; Wang, Z.; Li, X.; Chernova, N. A.; Chapman, K. W.; Zhou, G.; Piper, L.; Ong, S. P.; Whittingham, M. S. Rational Synthesis and Electrochemical Performance of $LiVOPO_4$ Polymorphs. *J. Mater. Chem. A* **2019**, *7* (14), 8423–8432.
10) Nojima, A.; Sano, A.; Fujita, S.; Ohtsuki, K.; Okada, S. Evaluation of α_1-$LiVOPO_4$, β-$LiVOPO_4$, and α-$LiVOPO_4$ Synthesized from a Same Precursor by Hydrothermal Method. *J. Electrochem. Soc.* **2019**, *166* (15), A3731–A3738.
11) Lii, K. H.; Li, C. H.; Cheng, C. Y.; Wang, S. L. Hydrothermal Synthesis, Structure, and Magnetic Properties of a New Polymorph of Lithium Vanadyl (IV) Orthophosphate: β-$LiVOPO_4$. *J. Solid State Chem.* **1991**, *95*, 352–359.
12) Barker, J.; Saidi, M. Y.; Swoyer, J. L. Electrochemical Properties of Beta-$LiVOPO_4$ Prepared by Carbothermal Reduction. *J. Electrochem. Soc.* **2004**, *151* (6), A796–A800.
13) Zhou, H.; Shi, Y.; Xin, F.; Omenya, F.; Whittingham, M. S. ε- and β-$LiVOPO_4$: Phase Transformation and Electrochemistry. *ACS Appl. Mater. Interfaces* **2017**, *9* (34), 28537–28541.
14) Liu, H.; Liu, H.; Lapidus, S. H.; Meng, Y. S.; Chupas, P. J.; Chapman, K. W. Sensitivity and Limitations of Structures from X-Ray and Neutron-Based Diffraction Analyses of Transition Metal Oxide Lithium-Battery Electrodes. *J. Electrochem. Soc.* **2017**, *164* (9), A1802–A1811.
15) Vincent, M. G.; Yvon, K.; Ashkenazi, J. Electron-Density Studies of Metal-Metal Bonds. II.* The Deformation Density of V_2O_3 at 295 K. *Acta Crystallogr. Sect. A* **1980**, *A36*, 803–808.

16) Lin, Y.-C.; Wen, B.; Wiaderek, K. M.; Sallis, S.; Liu, H.; Lapidus, S. H.; Borkiewicz, O. J.; Quackenbush, N. F.; Chernova, N. A.; Karki, K.; Omenya, F.; Chupas, P. J.; Piper, L. F. J.; Whittingham, M. S.; Chapman, K. W.; Ong, S. P. Thermodynamics, Kinetics and Structural Evolution of ε-$LiVOPO_4$ over Multiple Lithium Intercalation. *Chem. Mater.* **2016**, *28* (6), 1794–1805.
17) He, G.; Huq, A.; Kan, W. H.; Manthiram, A. β-$NaVOPO_4$ Obtained by a Low-Temperature Synthesis Process: A New 3.3 V Cathode for Sodium-Ion Batteries. *Chem. Mater.* **2016**, *28* (5), 1503–1512.
18) Enjalbert, R.; Galy, J. A Refinement of the Structure of V_2O_5. *Acta Crystallogr. Sect. A* **1986**, *C42*, 1467–1469.
19) Oka, Y.; Sato, S.; Yao, T.; Yamamoto, N. Crystal Structures and Transition Mechanism of VO_2(A). *J. Solid State Chem.* **1998**, *141* (2), 594–598.